nature portfolio

https://doi.org/10.1038/s41567-021-01193-4

Supplementary information

Unperturbed inverse kinematics nucleon knockout measurements with a carbon beam

In the format provided by the authors and unedited

Supplementary Materials for: Unperturbed inverse kinematics nucleon knockout measurements with a carbon beam

1. BM@N detector configuration. The BM@N experimental setup at JINR allows to perform fixed-target experiments with high-energy nuclear beams that are provided by the Nuclotron accelerator [1]. Our experiment was designed such that in particular protons under large laboratory angles can be measured. That dictated a dedicated upstream target position and modified setup as used for studies of baryonic matter, but using the same detectors [2]. The setup comprises a variety of detection systems to measure positions, times, and energy losses to eventually obtain particle identification and determine their momenta. We are using scintillator detectors, multi-wire proportional chambers, Silicon strip detectors, drift chambers, gas-electron multipliers, and resistive plate chambers as shown in Fig. 1 of the main text and described in the following.

Beam Counters (BC): A set of scintillator counters, each based on a scintillator plate with an air light guide viewed by a PMT, was installed in the beam line. Two counters (BC1 and BC2) were located before the target: BC1 was located at the beam entrance to the experimental area. It is a 15 cm in diameter and 3 mm thick scintillator read out by a XP2020 Hamamatsu PMT. BC2 was located right in front of the target and provided the start time t_0. This scintillator is of 4 cm x 6 cm x 0.091 cm size, and was tilted by 45° so that its effective area was around 4 cm x 4 cm. It was read out by a Photonis MCP-PMT PP03656. Two counters (BC3 and BC4), each read out by a XP2020 PMT, were located downstream the target to measure the total charge of the fragment particles in each event. BC3 was based on 10 cm x 10 cm x 0.29 cm scintillator, and the BC4 was 7 cm x 7 cm x 0.3 cm. A veto-counter with the dimensions of 15 cm x 15 cm x 0.3 cm and a hole of 5 cm in diameter was located between BC2 and the target. It was read out by an XP2020 PMT and was included in the reaction trigger to suppress the beam halo.

Multi-wire proportional chambers (MWPC): We used two pairs of MWPC chambers, one before and one after the target for in-beam tracking [3]. Each chamber has six planes $\{\mathrm{X}, \mathrm{U}, \mathrm{V}, \mathrm{X}, \mathrm{U}, \mathrm{V}\}$. The X wires are aligned in y direction, U and V planes are oriented ±60° to X. The distance between wires within one plane is 2.5 mm, the distance between neighboring planes is 1 cm. In total 2304 wires are read out. The active area of each chamber is 500 cm^2 (22 cm x 22 cm). About 1 m separated the chambers in the first pair upstream the target and 1.5 m between the chambers in the second pair downstream the target. The polar angle acceptance of the chambers downstream the target is 1.46°. The efficiency of the MWPC pair in front of the target for particles with the charge of 6 is (92.2±0.1)%. The efficiency of the MWPC pair after the target is (88.7±0.2)% for ions with $Z = 6$, and (89.3±0.2)%

for ions with $Z = 5$.

Silicon trackers (Si): As additional tracking system, three Silicon planes [4] were located after the target. In combination with the MWPCs after the target, an increased tracking efficiency is reached. The first and second Si planes share the same housing. The first plane consists of four modules, the second plane has two modules, the third plane has eight modules. Each module has 640 X-strips (vertical in y-direction) and 640 X'-strips (tilted 2.5° relative to X strips). The first plane has smaller modules with 614 X' strips and 640 X strips. The first two planes and the third plane are separated by 109 cm. The angular acceptance of the Si detector system is 1.58°. The design resolution of 1 mm for the y-coordinate and 50 μm for the x-coordinate was achieved in the experiment. The efficiency and acceptance of the Si tracking system, determined for reconstructed MWPC tracks before the target, is $(81.5 \pm 0.7)\%$ for outgoing $Z = 6$ ions, and $(82.6 \pm 0.7)\%$ for $Z = 5$ isotopes.

Combined tracks were reconstructed using information from the MWPC pair after the target and the Si detectors. The efficiency to find a Si track, and/or a track in the second pair of the MWPC, or a combined track is $(97.7 \pm 0.2)\%$ for $Z = 6$ ions, and $(97.9 \pm 0.3)\%$ for $Z = 5$ isotopes evaluated for events with reconstructed tracks upstream the target. For the fragment tracking additional matching conditions are required with downstream DCH tracks, as explained below, which ensures additional good track selection.

Drift Chambers (DCH): Two large-area drift chambers, separated by 2 m, are located downstream the bending magnet. These detectors are used for tracking the charged fragments in the forward direction. Together with the upstream-tracking information of MWPC and Si in front of the magnet, the bending angle and thus the magnetic rigidity of the ions is determined. Each chamber consists of eight coordinate planes, twice $\{\mathrm{X}, \mathrm{Y}, \mathrm{U}, \mathrm{V}\}$, where X wires are perpendicular to the x-axis, Y wires are at 90° relative to X, and U and V are tilted by $+/-45°$, respectively. The distance between wires within one plane is 1 cm, in total 12,300 wires are read out. The spatial resolution, given as residual resolution, for one plane (X, Y, U, or V) is around 200 μm (1σ). It is obtained by the difference between the measured hit and the position from the reconstructed track at that plane. The efficiency of around 98% (97%) for each plane was estimated for the first (second) DCH based on the reconstructed matched track in the second (first) DCH. A reconstructed track within one DCH chamber has at least 6 points.

Two-Arm Spectrometer (TAS): In order to detect light charged particles from the target, scattered to large laboratory angles, the symmetric two-arm detection system around the beamline was constructed for this experiment. Each arm, placed horizontally at $+/-29.5°$ (center) with respect to the beamline, was configured by the following

detectors along a 5 m flight length: scintillator – scintillator – GEM – RPC. Each arm holds one GEM (Gas-Electron Multiplier) station at a distance of 2.3 m from the target. Each GEM station contained two GEM planes with the dimensions of 66 cm (x) x 40 cm (y) each, placed on top of each other (centered at $y = 0$) to increase the overall sensitive area to 66 cm x 80 cm. The spatial resolution of the GEM hit is 300 μm. Each RPC detector station, located at the end of the two arms at a distance of 5 m from the target, has a sensitive area of 1.1 m x 1.2 m. Each station consists of two gas boxes next to each other, each holds 5 multi-gap Resistive-Plate Chambers (RPCs) planes inside [5]. Two neighboring planes within one box overlap by 5 cm in y direction. Each plane has 30 cm long 1.2 cm wide horizontally aligned readout strips with a pitch of 1.25 cm. The measured x position is obtained by the time difference measured between the ends of one strip. The resolution is 0.6 cm. Together with the position information from the GEM, tracks are reconstructed along the arms and the time-of-flight information is taken from the RPC system. The clustering algorithm was applied to the neighboring strips fired in the same event. In addition, each arm was equipped with two trigger counters (TC), scintillator planes close to the target. The X planes consisted of two scintillators with dimensions of 30 cm x 15 cm x 0.5 cm located vertically side by side and read out by a Hamamatsu 7724 PMT each. The distance between the target center and the X-counters was 42 cm. Each Y plane was a single scintillator piece of 50 cm x 50 cm x 2 cm, read out by two ET9954KB PMTs. The distance between the target center and the Y planes was 170 cm. Each arm covers a solid angle of 0.06 sr, limited by the RPC acceptance.

Data Acquisition System (DAQ) and Triggers: The DAQ performs readout of the front-end electronics of the BM@N detectors event-by-event based on the information of the trigger system [6]. Timing information were read out from DCH and RPC (two-edge time stamp) and processed by Time to Digital Converters (TDC) based on HPTDC chip with typical accuracy of 20 ps for RPC and 60 ps for DCH. The amplitude information were read out from coordinate detector systems of Si and GEMs and processed by Amplitude to Digital Converters (ADC). The last 30 μs of waveforms were read back. The clock and time synchronization was performed using White Rabbit protocol. As mentioned in the main text, the reaction trigger was set up requesting an incoming ion in coincidence with signals in the left and right arm trigger scintillator-counters (TC). Additional triggers are built from coincident signals in the various scintillator detectors, suited for either calibration purposes or data taking. The trigger matrix is shown in Table I, creating the so-called Beam trigger, and the physics triggers AndSRC and OrSRC. The input signals are BC1, BC2, and no veto signal (!V-BC). The coincidence condition AndXY requires signals in all TCs in the left and right arm, while OrXY takes the OR between the left and right arm of the spectrometer. The physics data were

taken requesting the AndSRC trigger at a rate of about 180 Hz as measured during a beam pulse duration, allowing a livetime close to 100%.

Supplementary Table I: | Trigger matrix. Different coincidence triggers for collecting the data.

Trigger	BC1	BC2	!V-BC	AndXY	OrXY
Beam	x	x	x		
AndSRC	x	x	x	x	
OrSRC	x	x	x		x

Data taking and quality: Signals from the TAS-TCs were combined with the BC and V-BC scintillator signals to form the main ^{12}C$(p, 2p)$ reaction trigger for the experiment. Additional triggers were set up for monitoring and calibration purposes, see Online Supplementary Materials for details.

The stability of the trigger was monitored online during the experiment as part of our data quality control. We collected and recorded about 20 million triggers. As part of the beam monitoring and quality, the ratio between BC2/BC1 and BC4/BC3 was not smaller than 65%, and the rate on the V-BC is on average 24% relative to BC2. The main ^{12}C$(p, 2p)$ reaction trigger had a rate of about 180 Hz, as measured during live beam. Variations of BC pulse height over the measurement time was monitored and accounted for in the analysis. No significant run-to-run variations were observed in any of the final observables.

2. Fragment momentum calculation Trajectories of charged particles are bent in the large analyzer magnet according to their magnetic rigidity $B\rho$, i. e. momentum-over-charge ratio $B\rho = P/Q$ with charge Q. This allows to determine the fragment total momenta.

For this purpose, simulations of the fragments, propagating in the magnetic field, were carried out using the field map of the magnet. The corresponding materials of the beam-line detectors were also implemented in the simulation. The simulated fragments were chosen to have the maximum possible position, angular and momentum spread to cover the entire geometrical acceptance of the magnet and detectors. The output of the simulation is used afterwards as a training sample for the multidimensional fit (MDF) algorithm [7] in the form of n-tuples which hold positions and angles of the fragment trajectory upstream and downstream of the magnet: $(x_0, y_0, z_0, \alpha_x, \alpha_y)$ and $(x_1, y_1, z_1, \beta_x, \beta_y)$ respectively. Performing MDF over the training sample yields an analytical fit function $P/Z^{mdf} =$

$f(x_0, y_0, z_0, \alpha_x, \alpha_y, x_1, y_1, z_1, \beta_x, \beta_y)$, which can be applied to the positions and angles measured in the experiment.

In a similar way, a second MDF function for α_x angle was derived as $\alpha_x^{mdf} = g(x_0, y_0, z_0, \alpha_y, x_1, y_1, z_1, \beta_x, \beta_y)$. This function is used for the track-matching condition $(\alpha_x^{mdf} - \alpha_x)$=min, which allows to determine whether the tracks in upstream and downstream detection systems belong to the same global track through the magnet.

Having determined the two functions, α_x^{mdf} and P/Z^{mdf}, experimental data for the reference trajectory of unreacted ^{12}C is used to adjust the input variables' offsets, which reflect the alignment of the real detectors in the experimental setup with respect to the magnetic field. This is achieved by variation of the offsets in the experimental input variables simultaneously for α_x^{mdf} and P/Z^{mdf} until the residual between P/Z^{mdf} and its reference value is minimal. The reference value is chosen to be the P/Z of unreacted ^{12}C at the exit of the liquid-hydrogen target. Using this approach a total-momentum resolution of 0.78 GeV/c for ^{12}C is achieved, as estimated with the empty target data, consistent with the resolution limits of the detection systems, see Fig. 2. The same momentum resolution was obtained for unreacted ^{12}C events, analyzed under the same conditions but with LH_2 target inserted. A width of $\sigma = 0.78$ GeV/c was measured with a reduced beam momentum of 47.6 GeV/c due to energy loss in the target and additional straggling. The achieved momentum accuracy is evaluated from simulation to be 0.2%.

Figure 1 shows the performance of the second MDF function for α_x. A global track is constructed when the reconstructed α_x^{mdf} falls within the 5σ gate indicated. In the analysis, only events with one heavy global track, which combines the up- and downstream detectors, are considered (if not stated differently). To ensure that real detected single-track events are selected, a matching between the upstream and DCH angle in y direction is applied together with the above explained x-angle matching, also in a 5σ selection from their residual. Additionally, a single track in the DCH, the one reconstructed track from DCH1 and DCH2, is required.

The fragment tracking efficiency is $(39.5^{+1.7}_{-2.6})\%$, obtained for an empty target run and given with respect to the incoming and outgoing $Z = 6$ ion. This tracking efficiency includes the involved detector efficiencies, as well as the reconstruction and matching efficiency of good single tracks. We define the tracking efficiency for ^{12}C as ratio of events, incoming carbon $^{12}C_{in}$ vs. carbon downstream the target $^{12}C_{out}$, with

$$\epsilon_{track} = \frac{\#^{12}C_{out}}{\#^{12}C_{in}} = \frac{\#(\text{Good track})\&(Z_{in} = 6)\&(Z_{eff} = 6)}{\#(Z_{in} = 6)\&(Z_{eff} = 6)}, \quad (1)$$

where a "good track" is defined by

- Tracks in one of the upstream detector systems and in DCH.

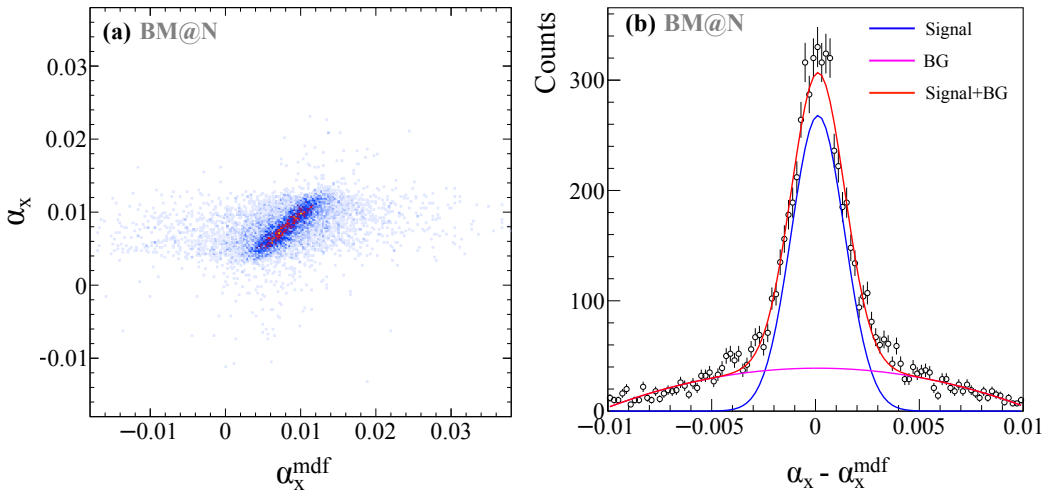

Supplementary Fig. 1: | **Track matching.** (a) Correlation between α_x angle measured upstream of the magnet and the α_x^{mdf} reconstructed by the MDF for unreacted ^{12}C beam . (b) Residual distribution $\alpha_x^{mdf} - \alpha_x$ fit with a Gaussian peak and wider underlying contribution ("BG" as second order polynomial).

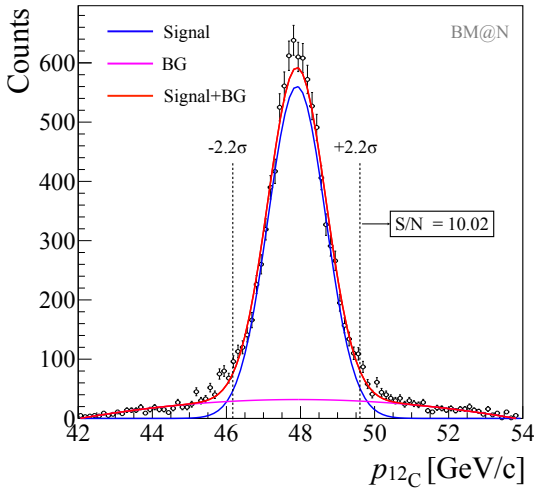

Supplementary Fig. 2: | **Fragment-momentum resolution.** Total momentum for ^{12}C measured with empty target, fitted with a Gaussian and possible underlying contribution ("BG"). The signal-to-noise ratio S/N is 10.0.

- Exactly one reconstructed matched global track based on the combined information from upstream detectors and DCH as explained above.
- A "good" P/Z value: for $^{12}C_{out}$ the P/Z value is expected to be centered around 7.98 GeV/c (for beam momentum of 47.9 GeV/c), cf. Fig. 2. The number of ^{12}C events corresponds to the integral in a $\pm 2.2\sigma$

range of P/Z, as applied on average for the fragment selection. The uncertainty to the tracking efficiency is determined from a $(2.2 \pm 0.45)\sigma$ range which reflects the range in P/Z selection for the different fragments of interest. In addition, we consider a systematic uncertainty coming from possible remaining wide tails in the P/Z distribution described by a second order polynomial. The signal-to-noise ratio is 10.0. That contribution creates an asymmetric uncertainty in the efficiency, considered on the 2σ level (cf. Fig. 2). This systematic uncertainty is considered in the same way for the quasielastic event yield, fitting the P/Z for the different charge selections.

Table II lists the different contributions to the extracted efficiency.

Supplementary Table II: The different contributions to the tracking efficiency.

Good track	$\epsilon_{\text{track}}(\%)$
$Z_{\text{in}} = 6$, $Z_{\text{eff}} = 6$	100
Upstream track	98
DCH track	93
Upstream and DCH tracks	91
Global track	70
Good P/Z	40

The tracking efficiency is reduced from 91% to 70% due to the MDF algorithm with the applied matching criteria in x angle and a reconstructed single global track. That event sample is further cleaned up requiring a single track in the DCH itself, and additional angular matching condition in the y direction (non-bending direction). See discussion above. Together with our analysis selection cuts of a good P/Z, the efficiency equals 40%. The reaction probability from in-beam material downstream the target was estimated to be smaller 5% and thus contributes only a small fraction in fragment misidentification. We estimated the uncertainty for B isotopes and ^{10}Be identification using the experimental data. We looked at the fraction of ^{11,10}B (^{10}Be) from events with $Z_{\text{eff}} = 5$ ($Z_{\text{eff}} = 4$). $Z_{\text{eff}} = 5$ are dominated by ^{11}B or ^{10}B. We varied the fragment identification cuts to check the sensitivity of this fraction. This resulted in a very similar uncertainty as for ^{12}C, and therefore we adapt the same uncertainty. $Z_{\text{eff}} = 4$ events are associated with several Be isotopes, or a combination of lighter fragments. In this case, to evaluate the uncertainty, we looked at the fraction of ^{10}Be from events with $Z_{\text{eff}} = 4$, and changed the identification cuts to evaluate the

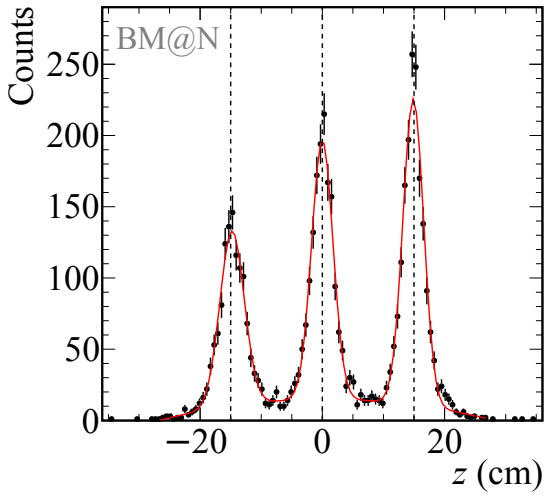

Supplementary Fig. 3: | TAS vertex. Vertex in z direction for 3 Pb foils at the target position to determine the position resolution of the vertex reconstruction. The position resolution is 1.8 cm (1σ), the fit is shown by the red line (plus background). The dashed black lines indicate the absolute position alignment at $z = \pm 15$ cm and zero.

sensitivity. This resulted in $\sim$ 15% difference (as opposed to 5% for C and B). Therefore, for ^{10}Be, we consider $\epsilon_{\text{track}} = (39.5^{+5.1}_{-7.8})\%$. For the overall fragment identification efficiency an additional $(83 \pm 6)\%$ efficiency for the measurement of the outgoing charge in BC3 and BC4 needs to be added.

3. Reaction-vertex reconstruction The reaction vertex is reconstructed whenever one track is reconstructed in each arm of the TAS. This requires at least one hit in the GEM and RPC systems to form a linear track in each arm. We consider only single-track options from the hit combinations. The coincident two tracks that come closest, formed from all possible hit combinations, determine the vertex position along the beam line in the z direction. Alignment procedures within the GEM-RPC system, the left and right arm, as well as relative to the incoming beam are applied. The initial detector positioning relied on a laser-based measurement, the alignment relative to the other detector systems and the beam using experimental data was done as mentioned before. The quality of the tracks is selected according to their minimum distance, a selection criteria of better than 4 cm is applied in this analysis. Given the smaller angular coverage of the RPC system compared to the GEMs and detector inefficiencies, the track reconstruction efficiency is 40%, with an RPC detection efficiency of about 85%.

The position resolution in z was determined by placing three Pb foils separated by 15 cm at the target position. The reconstructed vertex position is shown in Fig. 3, clearly three distinct peaks at a distance of 15 cm representing the Pb foils are reproduced. Given the width of each peak, the z-position resolution from the two-arm spectrometer

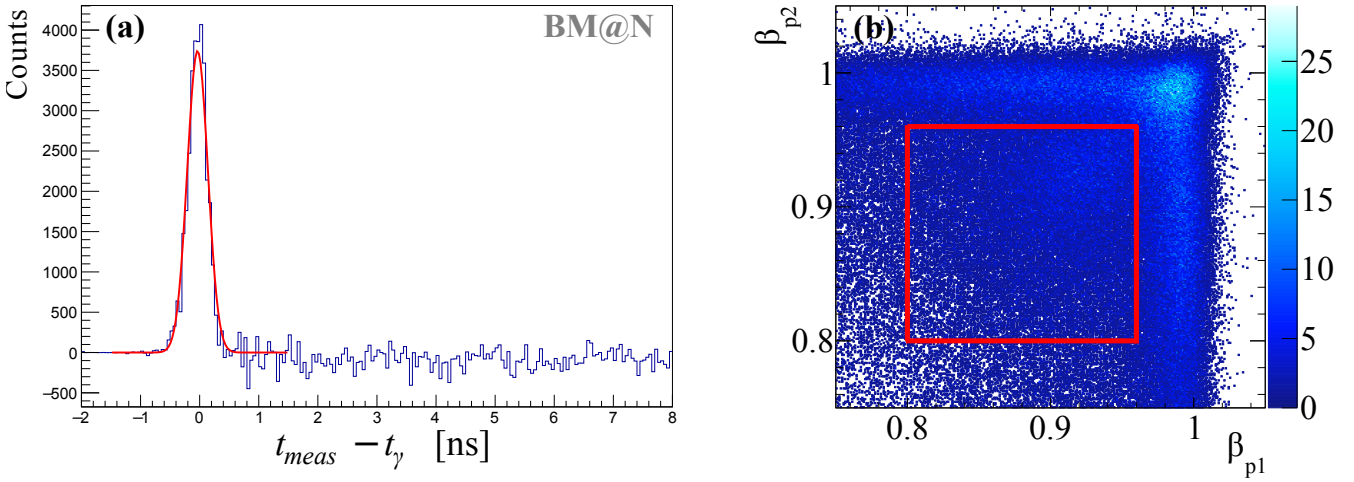

Supplementary Fig. 4: | TAS timing. (a) Result of RPC ToF calibration, γ peak arising in subtracted spectrum for Pb target runs with and without Pb sheets directly in front of RPC. The extracted ToF resolution is 175 ps $(1, \sigma)$. (b) Basic velocity condition to select protons, the velocity cut in the left and right arm are indicated by the red lines.

is on average 1.8 cm (1σ). Knowing the vertex and the track position in the RPC, the flight length is determined.

4. ToF calibration and proton momentum reconstruction resolution. The time-of-flight (ToF) calibration for the RPC is done by measuring gamma rays emitted from interactions with a single-foil Pb target. A 9 mm thick single Pb target was installed at the center position of the LH_2 target. In addition, a thin lead sheet was placed directly in front of the RPCs to convert gammas to charged particles. Measurements were done with and without the RPC lead sheet and the difference in the measured ToF spectrum for the two measurements was used to isolate gamma rays events. The subtracted ToF spectrum is shown in Fig. 4a, presenting a total ToF resolution (including the t_0 resolution) of 175 ps. Together with the time-of-flight that is measured between the start counter BC2 and the RPC, the total proton momentum can be determined. For a 2 GeV/c proton this corresponds to ΔToF/ToF $\sim 0.95\%$ which translates into a total-momentum resolution of 5.3% in the laboratory system and ~ 60 MeV/c for the missing momentum from the two protons in the ^{12}C rest frame.

Fig. 4b shows the β distribution of measured charged particles in the TAS with the initial velocity selection cut of $0.8 < \beta < 0.96$ applied for each particle shown as a red square.

5. Single-proton knockout data-analysis. The basic selection for any analysis requires an incoming ^{12}C, a good reaction vertex, and particles in the arms passing the velocity condition. These selections criteria define the inclusive

$(p, 2p)$ reaction channel, which is dominated by FSI and IE scattering. The exclusive reaction channel requires the additional detection of a ^{11}B fragment, with a single global-track condition and defines the one-proton QFS, that includes both QE and IE scattering.

We select a bound ^{11}B where the $3/2^-$ ground-state is populated with the largest cross section. However, we cannot distinguish bound excited states that de-excite via γ-ray emission that are also populated in our experiment. Previous works [8] found the contribution from such states to be small, coming primarily from the $1/2^-$ and $3/2^-$ states that contribute $\sim$10% each to the total cross section. This contribution also correspond to p-shell knockout and does not impact the resulting momentum distribution significantly.

In order to identify $(p, 2p)$ QE events and reject IE events, we look at the missing energy and the in-plane opening angle of the two particles measured in the arms. An elliptical cut denoted by $2\,\sigma$ is applied in each direction (Fig. 2 of the main text). The standard deviation was obtained from a Gaussian fit to E_{miss} ($\sigma = 0.108$ GeV) and $\theta_{p1} + \theta_{p2}$ ($\sigma = 1.8^\circ$).

The missing energy is defined as $E_{\mathrm{miss}} = m_p - e_{\mathrm{miss}}$, where e_{miss} is the energy component of $\bar{p}_{\mathrm{miss}}$ in the rest frame of the ^{12}C nucleus. The boost from the laboratory system into the rest frame is applied along the incoming-beam direction taking into account the reduced beam energy at the reaction vertex. The selection region for QE events is defined in the exclusive channel with fragment selection, in a 2σ ellipse as indicated in Fig. 2 of the main text. The IE part is defined from the remaining events within the other ellipse. The same criteria are applied in the inclusive channel. Correlations with other kinematical variables are shown in Extended Data Fig. 2.

The M^2_{miss} spectrum in Extended Data Fig. 3a shows the squared missing mass for the exclusive channel before and after applying the QE cut, clearly showing that we select background-free QE events with a missing mass that equals the proton mass. A lower boundary in the squared missing mass of $M^2_{\mathrm{miss}} > 0.47$ GeV$^2/c^4$ is applied. Since the chosen selection criteria might influence other kinematical variables of $\bar{p}_{\mathrm{miss}}$ (Eq. 2 of the main text), we show the momentum distributions and angular correlations with less strict selection in the Extended Data (Figs. 3, 4) which do not show a different behavior and are also described well by the simulation.

6. Single-proton knockout simulation. We compare the quasielastic ^{12}C$(p, 2p)^{11}$B data to a MonteCarlo simulation for the proton quasielastic scattering off a moving ^{12}C. In the calculation, the ^{12}C system is treated as spectator plus initial proton, $\mathbf{p}_{^{12}\mathrm{C}} = \mathbf{p}_{^{11}\mathrm{B}} + \mathbf{p}_i$. The proton's initial momentum distribution in ^{12}C is sampled from a theoretical distribution. Note that all kinematical quantities discussed here correspond to the carbon rest-frame.

The momentum distributions are calculated in the eikonal formalism for quasi-free scattering as described in Ref. [9]. In this work we compare the data to the momentum-distribution calculated without absorption effects, i. e. without multiple-scattering. Here we also compare to the same calculation that includes absorption effects from the imaginary part of the potential explicitly, calculated in the optical limit of Glauber theory. See in Extended Data Fig. 5.

The distorted waves are calculated from the real and imaginary part of the optical potential for the interaction between proton and nucleus. The single particle wave function of the removed proton is generated from a Woods-Saxon potential with radius given by $R = 1.2 \cdot A^{1/3}$ fm and diffuseness $a = 0.65$ fm, while the depth of the potential was adjusted to reproduce the removal energy, $S_p = 15.96$ MeV, of a proton from the $p_{3/2}$-shell. For the ^{12}C nucleus a density distribution from electron scattering was used as input, assuming that is has the same profile for the proton and neutron densities. The density is of the form $\rho_{^{12}\mathrm{C}} = (1 + \alpha \cdot (r/b)^2) \cdot \exp\left\{-r^2/b^2\right\}$, with $\alpha = 1.4$ and b chosen so as to reproduce the RMS radius of the ^{12}C, $b = 2.47$ fm.

Although the fragment selection removes events from FSI and we do not need to account for their scattering into measured phase space, we look at the calculation with absorption since the survival probability is larger if the knockout happens at the nuclear surface. This effect might create a difference from no distortions. However, the momentum distributions with and without absorption look very similar, see Extended Data Fig. 5, and do not seem to have a large impact on the reconstructed initial momentum distribution in a light system such as ^{12}C.

In terms of the kinematics, we raffle $|\mathbf{p}_i|$ from the total-momentum distribution and randomize its direction. The proton's off-shell mass is

$$m^2_{\mathrm{off}} = m^2_{^{12}\mathrm{C}} + m^2_{^{11}\mathrm{B}} - 2m_{^{12}\mathrm{C}} \cdot \sqrt{m^2_{^{11}\mathrm{B}} + \mathbf{p}_i^2}. \tag{2}$$

The two-body scattering between the proton in ^{12}C and the target proton is examined in their c.m. frame. The elastic-scattering cross section is parameterized from free pp differential cross section data. Following the scattering process, the two protons and ^{11}B four-momenta are boosted back into the laboratory frame.

The two-arm spectrometer was placed such that it covers the symmetric, large-momentum transfer, 90° c.m. scattering region. Given the large forward momentum, the detectors cover an angular acceptance of $\sim 24^\circ < \theta < 37^\circ$ in the laboratory system which corresponds to $\sim 75^\circ < \theta_{\mathrm{c.m.}} < 101^\circ$ in the c.m. frame.

In order to compare the simulated data to the experimental distributions, the simulation is treated and analyzed in the same way as the experimental data. Experimental acceptances are included. Resolution effects are convoluted to proton and fragment momenta. The proton time-of-flight resolution ΔToF/ToF is 0.95% at 2 GeV/c and the angular

resolution 5 mrad, while the fragment momentum resolution is 1.5% and the angular resolution 1.1 mrad in the x and y directions. The angular resolution of the incoming beam is 1.1 mrad. The beam-momentum uncertainty, examined as Gaussian profile, does not significantly impact rest-frame momentum distribution as long as the same nominal beam momentum is used for extracting physical quantities (or observables) from the experimental data and the simulated events. However, the momentum distributions are dominated by the width of the input p-shell momentum distribution. When comparing, the simulation is normalized to the integral of the experimental distributions. We find overall good agreement between experiment and Monte Carlo simulation showing that the reaction mechanism and QE events sample the proton's initial momentum distribution in ^{12}C. Additional data-simulation comparison is shown in Extended Data Fig. 4.

7. Multi-step QE-like contributions. As discussed above, the experiment measured the $\frac{^{12}\mathrm{C}(p,2p)^{11}\mathrm{B}}{^{12}\mathrm{C}(p,2p)}$ cross-section ratio. Due to the high-energy of our measurement, the $^{12}\mathrm{C}(p,2p)^{11}\mathrm{B}$ reaction is dominated by single-step scattering processes off p-shell nucleons whereas the $^{12}\mathrm{C}(p,2p)$ reaction include contributions from both single-step and QE-like multi-step processes off both p- and s-shell nucleons.

Theoretically, single-step reaction cross-sections can be calculated using a Glauber approximation that was previously shown to well reproduce high-energy transparency measurements for both $(p,2p)$ and $(e,e'p)$ data [10–12]. In contrast, calculations of QE-like multi-step processes are model dependent and sensitive to the exact experimental definition of QE events. Here we employ a Glauber approximation calculation following Ref. [9] which predicts the ratio of the single-step scattering cross-section off p-shell protons relative to that of both p- and s-shell protons, $\frac{(p,2p)^{p\ shell}_{single-step}}{(p,2p)^{p+s\ shell}_{single-step}} = 0.7$.

The contribution of QE-like multi-step processes to the measured $^{12}\mathrm{C}(p,2p)$ reaction prevents a direct comparison with the Glauber calculations of the single-step cross-section. However, by breaking the measured $\frac{^{12}\mathrm{C}(p,2p)^{11}\mathrm{B}}{^{12}\mathrm{C}(p,2p)}$ cross-section ratio to its different contributing processes as:

$$
\begin{aligned}
^{12}\mathrm{C}(p,2p)^{11}\mathrm{B} &= {}^{12}\mathrm{C}(p,2p)^{p\ shell}_{single-step}\ , \\
^{12}\mathrm{C}(p,2p) &= {}^{12}\mathrm{C}(p,2p)^{p+s\ shell}_{single-step} + \\
&\quad {}^{12}\mathrm{C}(p,2p)^{p+s\ shell}_{QE-like\ multi-step}\ ,
\end{aligned}
$$

we can use the measured cross-section ratio and the Glauber calculated single-step process cross-section ratio to

extract the fractional contribution of QE-like multi-step processes to the measured ^{12}C$(p,2p)$ cross-section:

$$\frac{^{12}\mathrm{C}(p,2p)^{p+s\ shell}_{QE-like\ multi-step}}{^{12}\mathrm{C}(p,2p)^{p+s\ shell}_{single-step} +^{12}\mathrm{C}(p,2p)^{p+s\ shell}_{QE-like\ multi-step}} =$$
$$1 - \frac{^{12}\mathrm{C}(p,2p)^{11}\mathrm{B}}{^{12}\mathrm{C}(p,2p)}|_{exp} \Big/ \frac{(p,2p)^{p\ shell}_{single-step}}{(p,2p)^{p+s\ shell}_{single-step}} = 0.376 \pm 0.084.$$

A semi-empirical estimate of this fraction can be obtained from Extended Data Fig. 5b where the excess of the data beyond the Glauber calculation accounts for 31% of the total ^{12}C$(p,2p)$ event yield. Here we take the missing-momentum distribution of the $(p,2p)^{p+s\ shell}_{sing.-step}$ process from the Glauber calculation, but normalize its yield to the data at low missing-momentum. Note that this extraction does not use the Glauber calculated 0.7 single-step p-shell scattering fraction as input, but still result in a QE-like multi-step fraction that is consistent with the one extracted using the measured and Glauber calculated cross-section ratios.

8. Selecting high-momentum SRC events. We study SRC events by focusing on ^{12}C$(p,2p)^{10}$B and ^{12}C$(p,2p)^{10}$Be events. We start with the two-proton detection imposing the vertex and β cuts mentioned above. The first cut applied to select SRC breakup events is to look at high-missing momentum, $p_{\mathrm{miss}} > 350$ MeV/c. This is guided by experimental scaling onset observation that indicate SRCs dominate above momenta of 275 ± 25 MeV/c, where the larger value is chosen to ensure that the measured events are above this onset momentum even after resolution smearing

The remaining event selection cuts are chosen following a GCF simulation of the ^{12}C$(p,2p)$ scattering reaction off high missing-momentum SRC pairs. After applying the high-missing momentum cut, we look at the in-plane opening angle between the protons for different cases: (a) inclusive ^{12}C$(p,2p)$ events, (b) GCF simulated SRC events, (c) exclusive ^{12}C$(p,2p)^{10}$B events, and (d) exclusive ^{12}C$(p,2p)^{10}$Be events. The GCF predicts relatively large opening angles that guides our selection of in-plane lab-frame opening angle larger than 63° (that also suppresses contributions from inelastic reactions that contribute mainly at low in-plane angles).

Next we apply a missing-energy cut to further exclude inelastic and FSI contributions that appear at very large missing-energies. To this end we examine the correlation between the missing energy and missing momentum, after applying the in-plane opening angle cut, for the full range of the missing momentum (i. e., without the $p_{\mathrm{miss}} >$ 350 MeV/c cut), see Extended Data Fig. 6. We chose to cut on $-110 < E_{\mathrm{miss}} < 240$ MeV.

To improve the selection cuts we use the total energy and momentum conservation in reactions at which we identified a fragment (^{10}B or ^{10}Be). We can write the exclusive missing-momentum in these reactions as

$$\bar{p}_{\mathrm{miss,excl.}} = \bar{p}_{^{12}\mathrm{C}} + \bar{p}_{tg} - \bar{p}_1 - \bar{p}_2 - \bar{p}_{^{10}\mathrm{B(Be)}}. \quad (3)$$

Neglecting the center-of-mass motion of the SRC pair, the missing-mass of this 4-vector should be equal to the nucleon mass $m^2_{\rm miss,excl.} \backsimeq m^2_N$. The distributions for ^{12}C$(p,2p)^{10}$B and ^{12}C$(p,2p)^{10}$Be events that pass the missing-momentum, in-plane opening angle, and missing-energy cuts are shown in Extended Data Fig. 7 together with the GCF simulation. To avoid background events with very small values of the missing-mass we choose to cut on $M^2_{\rm miss,excl.} > 0.42$ GeV^2/c^4. After applying this cut we are left with 23 ^{12}C$(p,2p)^{10}$B and 2 ^{12}C$(p,2p)^{10}$Be events that pass all the SRC cuts.

We note that if the measured SRC events were caused by FSI with a neutron in ^{11}B, we would expect to also detect a similar number of ^{10}Be fragments due to FSI with a proton in ^{11}B. At the high energies of our measurement these two FSI processes have almost the same rescattering cross sections [13]. Our measurement of only 2 ^{10}Be events is consistent with the SRC np-dominance expectation and not with FSI.

In addition, while our selection cuts suppress QE scattering events off the tail of the mean-field momentum distribution they do not completely eliminate them. Therefore, some events could result from de-excitation of high-$p_{\rm miss}$ ^{11}B fragments. Using the de-excitation cross-sections of Ref. [8] and the measured number of ^{12}C$(p,2p)^{11}$B events that pass our SRC selection cuts (except for the exclusive missing-mass cut), we estimate a maximal background of 4 ^{10}B and 2 ^{10}Be events due to knockout of mean-field protons and subsequent de-excitation.

9. Characterizing the selected ^{12}C$(p,2p)^{10}$B events. The majority of SRC events with a detected fragment comes with ^{10}B. In the Extended Data we present some kinematical distributions of these selected events together with the GCF simulation. Extended Data Fig. 8 shows the total ^{10}B fragment and missing moments as well as their different components. Overall good agreement between the data and simulation is observed.

The pair c.m. momentum width of $\sigma_{\rm c.m.} = (156 \pm 27)$ MeV/c was obtained from the distribution in the transverse direction to the beam by χ^2 comparison for several different c.m. width in the GCF simulation. The result is consistent with electron scattering measurements [14].

Due to the high momenta of the nucleons in SRC pairs, it is beneficial to also analyze the missing-momentum distribution in the relativistic light-cone frame where the longitudinal missing-momentum component is given by $\alpha = (E_{\rm miss} - p^z_{\rm miss})/m_p$. Similar to $p_{\rm miss}$, α is calculated in the ^{12}C rest frame where $\hat{z}$ is boosted target-proton direction. $\alpha = 1$ for scattering off standing nucleons. $\alpha < 1$ (> 1) corresponds to interaction with nucleons that move along (against) the beam direction and therefore decrease (increase) the c.m. energy of the reaction $\sqrt{s}$. Extended Data Fig. 9a shows the α distribution for the measured SRC events. We observe that $\alpha < 1$, as predicted by the

GCF and expected given the strong s-dependence of the large-angle elementary proton-proton elastic scattering cross-section. For completeness, Extended Data Fig. 9 also shows additional angular correlations between the nucleons in the pair and the ^{10}B fragment, all well reproduced by the GCF.

10. Estimating the number of SRC ^{12}C$(p,2p)^{10}$B and ^{12}C$(p,2p)^{10}$Be events. As a consistency check we performed a simple estimate of the expected number of exclusive SRC events based on the measured mean-field ^{12}C$(p,2p)^{11}$B event yield. We assume SRCs account for 20% of the wave function [15–17], and that their contribution to the exclusive measurements is suppressed by a factor of 2 as compared to the mean-field ^{12}C$(p,2p)^{11}$B due to the transparency of the recoil nucleon [10–12]. Therefore, we expect a contribution of 11% SRC and 89% mean-field.

The mean-field has contributions leading to bound states (i. e. p-shell knockout leading to ^{11}B) and continuum states (s-shell knockout, non-SRC correlations, etc.) with relative fractions of 53% and 36% respectively (53% + 36% = 89%) [8]. Therefore, given that we measured 453 ^{12}C$(p,2p)^{11}$B MF (p-shell knockout) events, we expect a total of $453 \cdot (11\%/53\%) = 94$ SRC events.

We estimate the experimental loss due to acceptance of the longitudinal momentum (see Extended Data Fig. 8a) as 50%, and another loss of 50% due to the strong cuts applied to select SRC events. Thus, in total, we expect to detect about $94 \cdot 50\% \cdot 50\% = 24$ SRC events.

If the SRC pair removal results in $A-2$ fragments close to its ground-state, and assuming np-dominance (20 times more np than pp pairs) we expect a population of 90% ^{10}B and 10% ^{10}Be. We also considered that for a pp pair the knockout probability is twice larger than for pn. Using the estimation of 24 total SRC events will lead to 22 events for ^{10}B (we measure 23) and 2 events for ^{10}Be (we measure 2). These simple estimates show overall self-consistency in our data.

Last, as our selection cuts suppress, but do not eliminate events originating from the tail of the mean-field distribution, some events could result from de-excitation of high-$p_{\rm miss}$ ^{11}B fragments. To evaluate that fraction, we consider ^{11}B events that pass the SRC selection cuts (except for the exclusive missing mass cut). 28 such events are observed of the total 453 MF ^{11}B events (i. e. a fraction of 9%). Reference [8] measured a neutron (proton) evaporation cross-section relative to the total continuum cross-section of 17% (7%). Using these fractions we expect a ^{10}B (^{10}Be) contribution from neutron (proton) evaporation based on the measured ^{11}B events of $(28/53\%) \cdot 36\% \cdot 17\% = 3$ events ($(28/53\%) \cdot 36\% \cdot 7\% = 1$). This is the maximum number that can be expected from this background, since for ^{10}B and ^{10}Be we apply an additional cut on the exclusive missing mass as explained above.

11. GCF simulations. The GCF was derived and validated against many-body Quantum Monte Carlo calculations in Refs. [17–19]. Its implementation into an event generator that can be used for analysis of experimental data is detailed in Ref. [20], and was successfully applied to the analysis of electron scattering SRC measurements in Refs. [20–23].

The $(p, 2p)$ cross-section expression for scattering off an SRC pair is give by:

$$\frac{d^8\sigma}{dtd\phi^* dp_{rel} d^2\mathbf{\Omega}_{rel} d^3\mathbf{p}_{CM}} = K\frac{1}{2\pi}\frac{d\sigma^{pp}}{dt}\sum_{\alpha,N} C^{\alpha}_{pN}\frac{|\tilde{\phi}^{\alpha}_{pN}(p_{rel})|^2}{(2\pi)^3}p^2_{rel}n(p_{CM}),$$

Where p_{rel} and p_{CM} are the SRC pair relative and center-of-mass momentum, C^{α}_{pN} are nuclear contacts defining the number of SRC pairs of type pN (= pp, pn) and spin α (= 0, 1). σ_{pp} is the proton-proton elastic scattering cross-section. $n(p_{CM})$ is a three-dimensional Gaussian describing the total pair momentum distribution. $\tilde{\phi}^{\alpha}_{pN}(p_{rel})$ is the pair relative momentum distribution given by the zero-energy solution of the two-body Schrödinger equation using the AV18 potential. K is a kinematical factor.

The adaptation of the GCF event generator from $(e, e'p)$ reaction cross-section [20], to the $(p, 2p)$ reactions using the above cross-section is simple and mainly required replacing the electron mass with a proton mass when calculating the reaction kinematics and phase-space factors and replacing the elementary electron-nucleon cross-section by the elastic proton-proton cross-section used in the mean-field simulation discussed above. We accounted for the experimental acceptance and detector resolution in the same way as described for the mean-field simulation discussed above.

The input parameters of the GCF calculation include: an NN interaction model, for which we used the $AV18$ interaction; consistent nuclear contact terms, that were adopted from Ref. [19]; the width of the SRC pair c.m. momentum distribution, which we set equal to $\sigma^{\rm GCF}_{\rm c.m.} = 150$ MeV/c [14]; and an $A-2$-system excitation energy, which we set to zero.

The uncertainty on the GCF calculation stems from uncertainties in the values of the nuclear contact terms (see Ref. [19]), $\sigma^{\rm GCF}_{\rm c.m.} = \pm 20$ MeV/c, and the $A-2$-system excitation energy. The latter was taken as equal to 2 or 5 MeV, with an abundance of 10% each.

[1] Kapishin, M. Studies of baryonic matter at the BM@N experiment (JINR). *Nucl. Phys. A* **982**, 967–970 (2019).

[2] Conceptual design report BM@N – Baryonic Matter at Nuclotron (2013).

[3] Khabarov, S. et al. First glance at the tracking detectors data collected in the first BM@N SRC run. *EPJ Web Conf.* **201**, 04002 (2019).

[4] Kovalev, Y. et al. Central tracker for BM@n experiment based on double side si-microstrip detectors. *Journal of Instrumentation* **12**, C07031 (2017).

[5] Babkin, V. et al. Triple-stack multigap resistive plate chamber with strip readout. *Nucl. Instrum. Meth. A* **824**, 490–492 (2016).

[6] BM@N DAQ system (2020). https://afi.jinr.ru

[7] ROOT Cern: Multi-dimensional fit. https://root.cern.ch/doc/master/classTMultiDimFit.html.

[8] Panin, V. et al. Exclusive measurements of quasi-free proton scattering reactions in inverse and complete kinematics. *Phys. Lett. B* **753**, 204–210 (2016).

[9] T. Aumann, C.A. Bertulani, and J. Ryckebusch. Quasifree $(p, 2p)$ and (p, pn) reactions with unstable nuclei. *Phys. Rev. C* **88**, 064610 (2013).

[10] D. Dutta, K. Hafidi, and M. Strikman. Color Transparency: past, present and future. *Prog. Part. Nucl. Phys.* **69**, 1–27 (2013).

[11] O. Hen et al. Measurement of transparency ratios for protons from short-range correlated pairs. *Phys. Lett. B* **722**, 63–68 (2013).

[12] M. Duer et al. Measurement of Nuclear Transparency Ratios for Protons and Neutrons. *Phys. Lett. B* **797**, 134792 (2019).

[13] Alkhazov, G.D., Belostotsky, S.L. & Vorobev, A.A. Scattering of 1-GeV Protons on Nuclei. *Phys. Rept.* **42**, 89–144 (1978).

[14] Cohen, E. O. et al. Center of Mass Motion of Short-Range Correlated Nucleon Pairs studied via the $A(e, e'pp)$ Reaction. *Phys. Rev. Lett.* **121**, 092501 (2018).

[15] Egiyan, K. et al. Measurement of 2- and 3-nucleon short range correlation probabilities in nuclei. *Phys. Rev. Lett.* **96**, 082501 (2006).

[16] Wiringa, R. B., Schiavilla, R., Pieper, S.C. & Carlson, J. Nucleon and nucleon-pair momentum distributions in $a \leq 12$. *Phys. Rev. C* **89**, 024305 (2014).

[17] Weiss, R., Cruz-Torres, R., Barnea, N., Piasetzky, E. & Hen, O. The nuclear contacts and short range correlations in nuclei. *Phys. Lett. B* **780**, 211 (2018).

[18] Weiss, R., Bazak, B. & Barnea, N. Generalized nuclear contacts and momentum distributions. *Phys. Rev. C* **92**, 054311 (2015).

[19] Cruz-Torres, R. et al. Many-Body Factorization and Position-Momentum Equivalence of Nuclear Short-Range Correlations. *Nature Physics* (2020).

[20] Pybus, J. R. et al. Generalized Contact Formalism Analysis of the ^{4}He$(e, e'pN)$ Reaction. *Phys. Lett. B* **805**, 135429 (2020).

[21] Weiss, R., Korover, I., Piasetzky, E., Hen, O. & Barnea, N. Energy and momentum dependence of nuclear short-range correlations - Spectral function, exclusive scattering experiments and the contact formalism. *Phys. Lett. B* **791**, 242–248 (2019).

[22] Duer, M. et al. Direct Observation of Proton-Neutron Short-Range Correlation Dominance in Heavy Nuclei. *Phys. Rev. Lett.* **122**, 172502 (2019).

[23] Schmidt, A. et al. Probing the core of the strong nuclear interaction. *Nature* **578**, 540–544 (2020).